



Article

# Sensors on Flapping Wings (SOFWs) Using Complementary Metal–Oxide–Semiconductor (CMOS) MEMS Technology

Lung-Jieh Yang <sup>1</sup>, Wei-Cheng Wang <sup>1,\*</sup>, Chandrashekhar Tasupalli <sup>1</sup>, Balasubramanian Esakki <sup>2</sup> and Mahammed Inthiyaz Shaik <sup>1</sup>

<sup>1</sup> Department of Mechanical and Electromechanical Engineering, Tamkang University, New Taipei City 251, Taiwan; ljyang@mail.tku.edu.tw (L.-J.Y.); chandrasekharamma25@gmail.com (C.T.); shaikinthyaz054@gmail.com (M.I.S.)

<sup>2</sup> Department of Mechanical Engineering, National Institute of Teaching Teachers Training and Research, Chennai 600113, India; esak.bala@gmail.com

\* Correspondence: bmw001234567@gmail.com; Tel.: +886-939712377

**Abstract:** This article presents a framework of using MEMS sensors to investigate unsteady flow speeds of a flapping wing or the new concept of sensors on flapping wings (SOFWs). Based on the implemented self-heating flow sensor using U18 complementary metal–oxide–semiconductor (CMOS) MEMS foundry provided by the Taiwan Semiconductor Research Institute (TSRI), the compact sensing region of the flow sensor was incorporated for in situ diagnostics of biomimetic flapping issues. The sensitivity of the CMOS MEMS flow sensor, packaged with a parylene coating of 10  $\mu\text{m}$  thick to prolong the lifetime, was observed as  $-3.24 \text{ mV/V}/(\text{m/s})$ , which was below the flow speed of 6 m/s. A comprehensive investigation was conducted on integrating CMOS MEMS flow sensors on the leading edge of the mean aerodynamic chord (m.a.c.) of the flexible 70-cm-span flapping wings. The interpreted flow speed signals were checked and demonstrated similar behavior with the (net) thrust force exerted on the flapping wing, as measured in the wind tunnel experiments using the force gauge. The experimental results confirm that the in situ measurements using the concept of SOFWs can be useful for measuring the aerodynamic forces of flapping wings effectively, and it can also serve for future potential applications.

**Keywords:** sensors on flapping wings (SOFWs); flow sensor; CMOS MEMS; flapping wing



Academic Editor: Huanyu Cheng

Received: 3 December 2024

Revised: 23 December 2024

Accepted: 10 January 2025

Published: 14 January 2025

**Citation:** Yang, L.-J.; Wang, W.-C.; Tasupalli, C.; Esakki, B.; Shaik, M.I. Sensors on Flapping Wings (SOFWs) Using Complementary Metal–Oxide–Semiconductor (CMOS) MEMS Technology. *Eng* **2025**, *6*, 15. <https://doi.org/10.3390/eng6010015>

**Copyright:** © 2025 by the authors. Licensee MDPI, Basel, Switzerland. This article is an open access article distributed under the terms and conditions of the Creative Commons Attribution (CC BY) license (<https://creativecommons.org/licenses/by/4.0/>).

## 1. Introduction

The micro air vehicle (MAV) is one of the modern technologies, which was developed as a branch of unmanned air vehicles (UAVs) over the decades. The biomimetic flapping wing micro aerial vehicle (FWMAV) synchronously flaps the wings to produce lift and thrust forces for forward flight and hovering. During the upstroke and downstroke motions, the lift and thrust forces of a flapping bird constantly change, and the aerodynamic forces are generated for efficient maneuvering. It creates a curiosity among the researchers for an onsite force measurement of the flapping wings. Micro-electro-mechanical systems (MEMS) sensors are an excellent choice for measuring the dynamic forces with respect to time. The most notable FWMAVs are Microbat [1], Delfly [2], Nano Hummingbird [3], and Konkuk Beetle [4]. They have potential advantages for challenging missions, including disaster relief and military operations.

With a commitment to pushing the boundaries of FWMAV technology forward, new flapping wing designs stand as a testament to expertise, innovation, and a dedication to advancing the capabilities for a wide range of practical applications. Therefore, the

FWMAV research delves into the nuanced interplay of a few factors and its effects on the performance of flapping airfoils. By examining variations in Reynolds number, thickness, and camber, the study provides valuable insights into optimizing airfoil designs for efficient propulsion, contributing to advancements in the understanding of fluid–structure interactions [5]. The various research investigations aim to enhance the MAV’s aerodynamic performance and provide valuable insights into tailoring wing configurations to achieve superior aerodynamic efficiency, e.g., by morphing wings [6], corrugation wings [7] via their intrinsic aspects of tailless configurations, to increase the flapping stroke angle [8], etc.

Wind tunnel testing epitomizes the general method of global lift and thrust forces measurement for aircraft [9], including FWMAVs. The particle image velocimetry (PIV) [10] and flow visualization [11] demonstrated the detailed internal flow field characteristics of FWMAVs. In addition, the flow sensor on airframe wing surfaces has the merits of direct signal acquisition, fast processing, efficient integration of on-board avionics, and real-time aerodynamic information feedback to the UAV/FWMAV flight control in the future.

In the 1990s, Ho and Tai developed a flow sensor using MEMS technology to study the low Reynolds number microchannel flow characteristics with reference to pressure variation [12]. It provided an indispensable resource for fundamental flow sensor design by highlighting the nonlinear nature of pressure distribution within uniform microchannels, thereby contributing valuable insights into the fundamentals of fluid mechanics [13]. Their work elucidates the principles and performance of these microscale sensors. It also involves the design, fabrication, and functionality of polysilicon-based micromachined hot wire-type anemometers, providing a valuable resource for researchers and engineers in the field of flow measurement and microsensor technology [14]. Regarding the operating principle of flow sensors, e.g., it depends on the interior of the micro-mechanic structure with a specific geometry and integrated circuit arrangement. To achieve this, the research group at the University of California Los Angeles (UCLA) and Caltech delved into the inventive design of a parylene-based skin equipped with adaptive check valves [15]. This technology exhibited a promising applications demanding dynamic flow control, as expounded in the succinct proceedings. It provided a novel method of application in separation point detection by creating a flexible sensor array proficient in detecting shear stress [16]. In addition, the continued innovative advancements in MEMS sensor development have garnered significant attention, with investigations adeptly exploring their effective deployment for vortex control and illustrating potential applications in bolstering aerodynamics and refining aircraft performance [17]. In summary, the evolution of this pioneering sensor technology yields to more intensive applications towards the aerodynamic measurement of FWMAV [18].

One author developed on-site lift measurements using polyvinylidene fluoride (PVDF) piezoelectric film on the flapping wings, which is different from the UCLA/Caltech’s discrete sensor/actuator array technique [9]. The PVDF film is integrated in the flapping wing membrane, and on-site measurement of aerodynamic forces was performed. It provided the total lift force as a real-time global output, and it was not able to detect air drag or thrust information due to its piezoelectric characteristic. In addition, Javed et al. meticulously examined the fundamental concepts underlying MEMS pressure-sensing technology, offering insights into its theoretical foundations [19]. Emphasizing aerospace applications, the review covered the integration of MEMS pressure sensors in various contexts, illustrating their relevance and potential impact on aerospace systems.

It is evident that the MEMS sensors used in on-site measurement are mostly pressure sensors and tactile force sensors, and flow sensors were not much utilized, except in the work of Ho and Tai [14–18]. Regarding MEMS sensors, Nguyen conducted a concise rigorous review focusing on various applications [20]. Dalola detailed the integration of a

MEMS thermal flow sensor with an intelligent electronic interface, emphasizing advancements in sensor technology and its potential applications across various domains [21]. Wu explored the advancements in MEMS technology for thermal flow sensors, providing a comprehensive overview of their principles and applications [22]. These findings contribute to the ongoing development of MEMS-based sensor technologies in fluid dynamics. Meanwhile, the various studies showcased the advancements in combining complementary metal–oxide–semiconductor (CMOS) and MEMS technologies, resulting in a sensor with enhanced performance capabilities for varied flow conditions. The detailed advancements in the development and utilization of these sensors contributes to the ongoing progress in microsensor technologies for flow measurements, which can be seen in [23,24].

The application of MEMS-based flow sensors for onsite measurements need proper packaging of the whole sensing framework. Xu et al. examined diverse packaging issues and their impact on the efficiency of CMOS calorimetric flow sensors [25]. It offered valuable insights into refining packaging strategies to augment the collective performance of these sensors. Similarly, Dumstorff et al. [26] also delved into advancements in packaging techniques, shedding light on their role in optimizing the operational efficiency of membrane-based thermal flow sensors.

The commercialized MEMS flow sensors are always properly packaged to deal with environmental contamination and long lifetime issues. In addition, incorporating these sensors into the tiny spaces of drones and even on the wing surfaces without degrading the output performance of the flow sensor was hard, and very few research works being carried out focus on this [27]. Therefore, it is inevitable to reinvestigate the onsite measurement of the flow fields around drones, flapping wings, or even rotating turbines [28] by redesigning and fabricating the MEMS flow sensors to meet the needs of the current engineering systems.

In this article, the authors proposed to incorporate MEMS-based sensors on flapping wings (SOFWs) to verify the aerodynamic performance characteristics of FWMVs. Figure 1 shows the integration of CMOS MEMS sensors on a flapping wing.

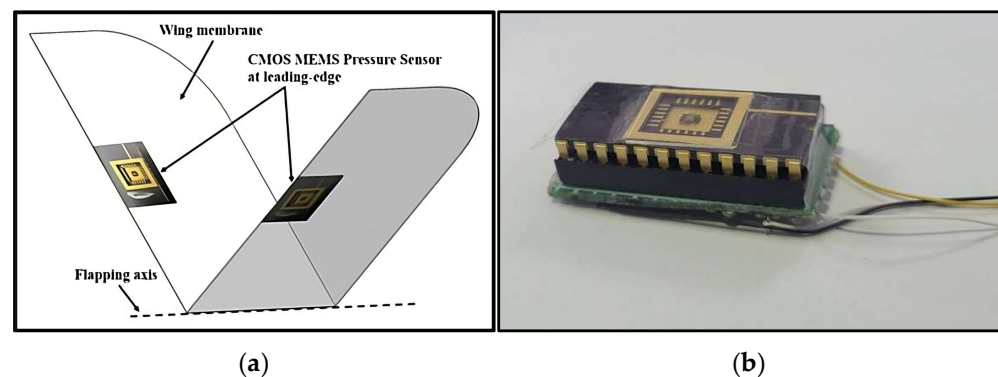


**Figure 1.** Integration of CMOS MEMS sensors on a flapping wing: (a) Concept of the MEMS sensors on flapping wings (SOFWs). (b) CMOS MEMS flow sensor unit.

The Taiwan Semiconductor Research Institute's (TSRI's) foundry service of CMOS MEMS technology was utilized for the fabrication of a MEMS sensor for efficient and quick fabrication in comparison to conventional fabrication [29–31].

## 2. Materials and Methods

### 2.1. CMOS MEMS Flow Sensor Measurement and Calibration in a Small Wind Tunnel

The hot wire-type CMOS MEMS flow sensors was fabricated through adopting the United Microelectronics Corporation (UMC) 0.18  $\mu\text{m}$  CMOS MEMS process with the multiple project wafer (MPW) service provided by TSRI [31]. The novel flow sensor with

the die size of  $1.5 \text{ mm} \times 1.5 \text{ mm}$  incorporated with the self-heating resistive thermal detector (RTD) for sensing the flow speed was fabricated. It was wire-bonded and mounted in a conventional dual-in-line package (DIP) shown in Figure 2a,b.

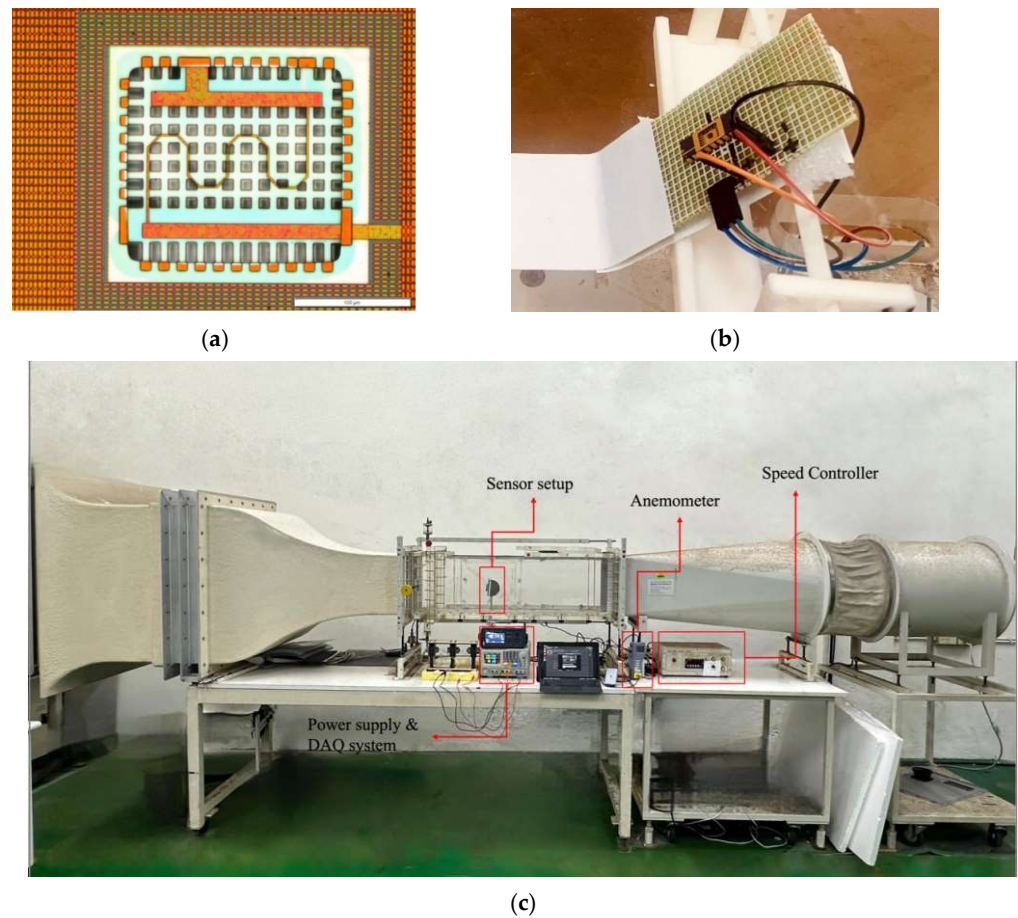


**Figure 2.** (a) Single-chip die of the CMOS MEMS flow sensor [28]. (b) Flow sensor chip laid on a slope with a  $60^\circ$  inclined angle or installation angle relative to upstream [28]. (c) Low-speed wind tunnel experimental setup.

The CMOS MEMS flow sensor, post-packaging, underwent validation within a low-speed wind tunnel. Calibration spanned wind speeds from 0 to 15 m/s, while the sensor, encapsulated and biased at 1.8 V, was positioned at an inclined angle of  $60^\circ$ . The installation angle of the flow sensor is shown in the “Sensor setup” of Figure 2. The wind tunnel, with a test section measuring  $30 \text{ cm} \times 30 \text{ cm} \times 100 \text{ cm}$ , facilitated the experimentation. In Figure 2c, the experimental setup showcases the application of a 1.8 V bias voltage to half-bridge RTDs ( $1 \text{ K}\Omega$  each). The RTDs exhibited a total self-heating power of 1.62 mW. In addition, the wind tunnel’s impact on the flow sensor’s temperature change was minimal.

To ascertain sensor repeatability, three consecutive tests were conducted for each wind speed, involving a 2-min data acquisition period and a subsequent 1-min rest interval. Utilizing the half-bridge circuit during testing, the output voltage signals were recorded and subsequently stored in Excel format. Post-wind tunnel testing, the output voltages underwent averaging to derive the mean values. These mean values were then plotted, accounting for each sensor configuration and wind speed. Wind tunnel trials were conducted thrice for the original sensor, with output voltages meticulously documented. It is imperative to note that the measured output voltages manifested in alternating current (AC) form, showcasing dynamic behavior. Each test had a standardized duration of 2 min, resulting in a total of 250 scans. The mean output voltage values, representative of each

wind velocity, were systematically computed, contributing to the comprehensive evaluation of the CMOS MEMS flow sensor’s performance under varied wind conditions.

Based on the laminar thermal boundary layer theory and the half-bridge hot wire flow sensing principle, and after substituting all dimensions and property values, the theoretical relationship between the flow speed  $u$  in m/s and the output voltage  $V_{out}$  for the flow sensor is derived as [31].

$$V_{out} = (0.9) \left[ 1 + \frac{69.02}{u + (1265)\sqrt{u} + 2389} \right] [\text{Volt}]; \tag{1}$$

After testing the sensor under different inclined angles, the data stored in Excel need to be processed in MATLAB (R2022a) to eliminate the external noises produced during the testing by using a cutoff frequency code. After processing the data through MATLAB, the data points were averaged; this task is performed for each wind velocity ranging from 1 to 6 m/s for the inclined angles ranging from 20 to 60° by the stand in Figure 3a. The final results of the calibration test after processing all data individually were plotted together, which is shown in Figure 3b.

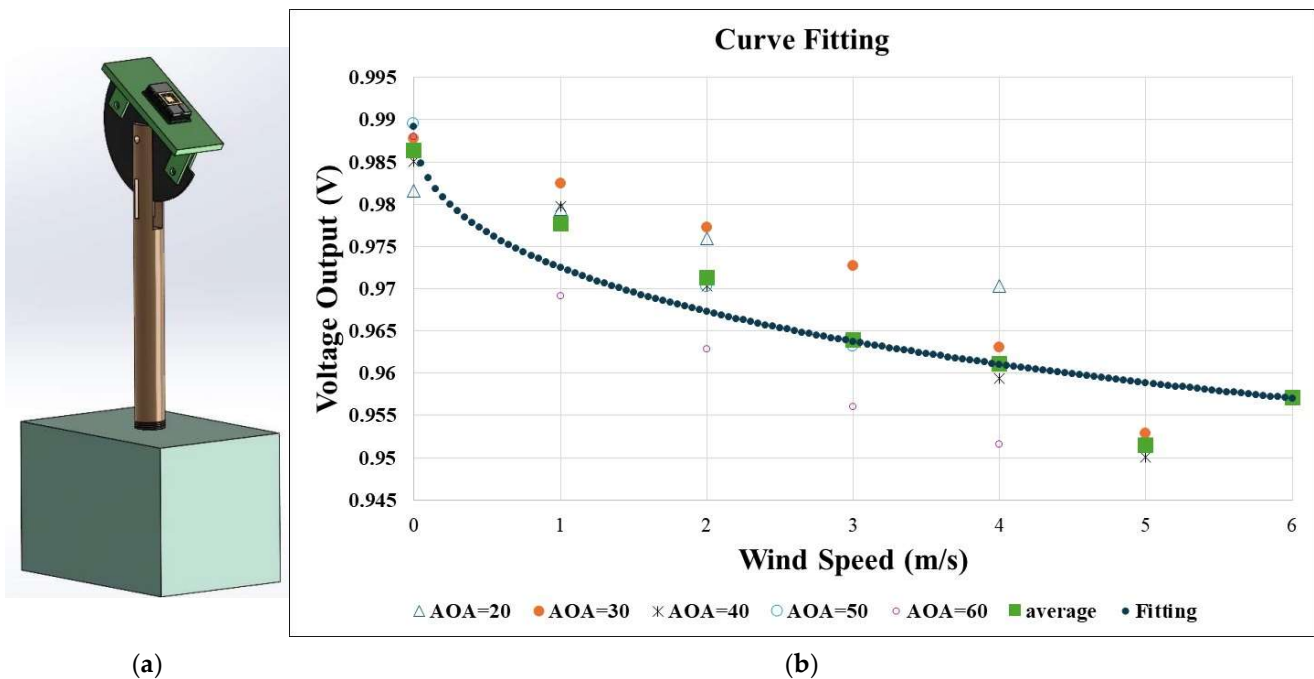


**Figure 3.** Stand for calibrating flow sensor output according to different inclined angles: (a) 3D design; (b) measured data points with different inclined angles from 20° to 60° and the fitting curve of Equation (3) using the least squares error method to denote the measured data trend. The sensitivity of the CMOS MEMS flow sensor is  $-3.24 \text{ mV/V/(m/s)}$ . If the linear fitting is applied to evaluate the sensitivity of the CMOS MEMS flow sensor, it may cause 30~40% maximum uncertain deviation of the flow speed measurement on the flapping wings because of the nonlinear relationship between the output voltage and the flow speed in Equations (1)–(3).

Upon analyzing the calibration versus wind speed at various inclined angles, as shown Figure 2b, it becomes apparent that the sensor output voltage exhibited a monotonic trend with changes in the angle of attack (AOA). Consequently, the most straightforward method for calibrating the sensor involves modeling the relationship between the sensor output voltage and the wind speed in a manner analogous to the theoretical relation given in Equation (1). To restate, the lack of a monotonic relationship suggests that the sensor’s response to changes in the inclined angle is complex and nonlinear. Therefore, correlating the output voltage with the AOA may lead to inaccuracies and inconsistencies in the data.

Instead, by focusing on the wind speed and its impact on the sensor output, we may develop a more reliable calibration model. This approach entails deriving an empirical relationship that aligns closely with the theoretical relations given in Equation (1).

$$V_{out} = (V_o/2) \left[ 1 + \frac{a}{u + b\sqrt{u} + c} \right] \quad (2)$$

where  $a$ ,  $b$ , and  $c$  represent the undetermined coefficients. If the condition  $u \ll b\sqrt{u}$  holds, then Equation (2) can be further simplified as

$$V_{out} = (V_o/2) \left[ 1 + \frac{A}{B\sqrt{u} + 1} \right] \quad (3)$$

In order to find out the theoretical coefficients  $A$  and  $B$  by using the least squares error method, a fitting curve was plotted, as shown in Figure 3. With coefficients of  $A = 0.43$  and  $B = 4.34$ , Equation (3) was used to convert the sensor voltages into the local speed values during the flapping wing testing experiments using a medium-sized wind tunnel.

Based on the derived regression line and trend of the data points analysis, it was evident that the ideal wind speed was set to be within the range of 0 to 6 m/s. The fitting curve distribution, as shown in Figure 3b, demonstrated that the maximum deviation between the fitting curve and the original data points was approximately 1% to 4%. To rationalize the theoretical values with the real-time data, the sensor output was compared to the theoretical data. The actual data points with an error exceeding  $\pm 2\%$  were prioritized for removal. The result indicated that the optimal data measurement fell within the AOA range of 20 to 60 degrees, which also matched with the instantaneous AOA values measured in [32].

## 2.2. The MEMS SOFWs in a Medium-Sized Wind Tunnel

The CMOS MEMS sensors were integrated to the flapping wings, and they were expected to dynamically measure the output voltage from the flapping motion, which, in turn, estimate the aerodynamic forces produced by a flapping wing. Generally, a load cell or a six-axis force–moment gauge (45E15A4) was used to obtain the lift and net thrust force from a flapping motion [9] using the wind tunnel experimental setup shown in Figure 4. The load cell can provide a dynamic output signal with respect to the flapping motion, and a certain calibration matrix helps to convert the electrical signals into unsteady data points of lift and net thrust forces of a flapping wing at different inclined angles [9].

Two flapping wings of a 70-cm-span with the configurations A1 and A2 integrated with the CMOS MEMS flow sensors on the wings were prepared, as shown in Figure 5. The CMOS flow sensors were assigned as S1 and S2 on the configuration of A1 and as B1 and B2 on the configuration of A2. Four calibration curves are obtained for the output voltages for CMOS MEMS flow sensors such as S1, S2, B1, and B2 mounted on the wings. These sensors were positioned on the m.a.c. [33] and at the leading edge of the flapping wing.

In the realm of CMOS MEMS flow sensors, the original time-changing signal waveforms correspond to the dynamic variations in flow rates or velocities sensed by the device. These waveforms capture the intricate fluctuations in the fluid flow, reflecting changes in the velocity or mass flow rate over time. During the data acquisition process in CMOS MEMS flow sensors, the analog signals are generated by the sensor in response to the fluid flow, which are converted into discrete digital data points. This conversion is crucial for subsequent processing and analysis. To enhance the reliability of the signal and reduce the impact of noise or transient disturbances, these digital data points were often subjected to time-averaging algorithms within the data acquisition (DAQ) system. The transformation to average data points involves calculating the mean value of a set of consecutive data

points over a specified time interval and neglecting the inertial force during the flapping motion [9].

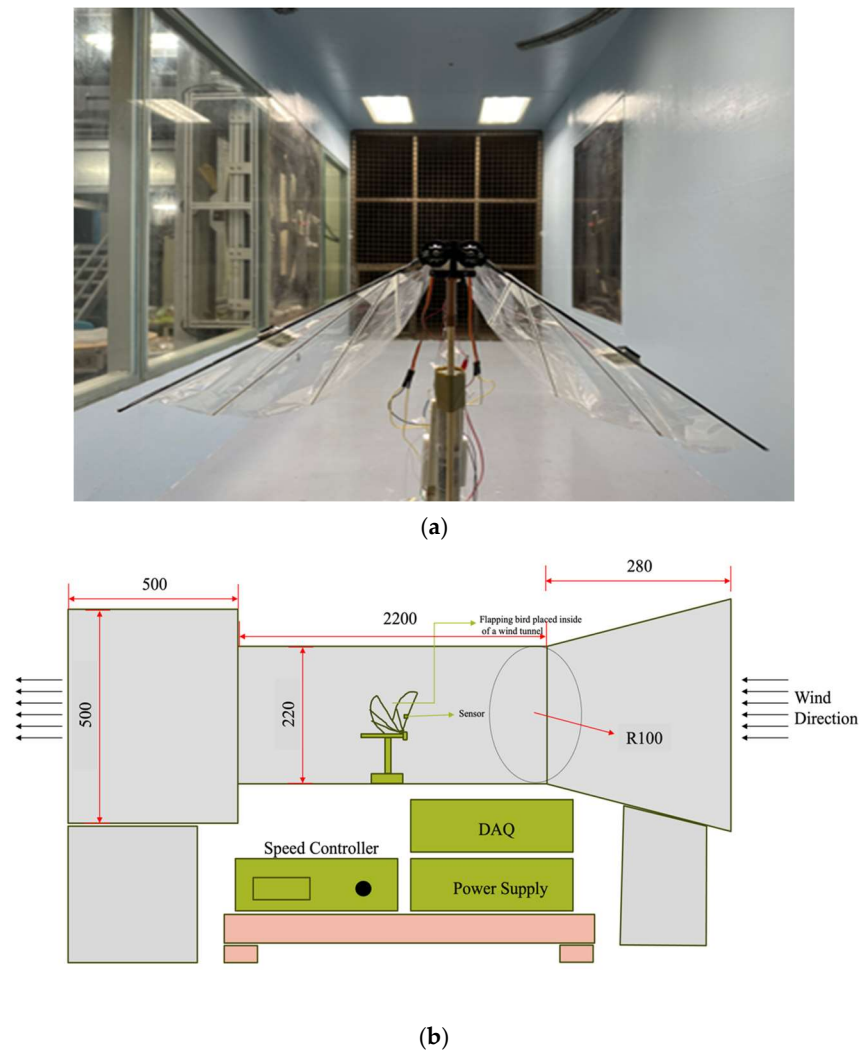


**Figure 4.** (a) Scenario concept of SOFWs in a medium-sized wind tunnel. (b) The dimensions of the medium-sized wind tunnel different from the small wind tunnel in Figure 2c.

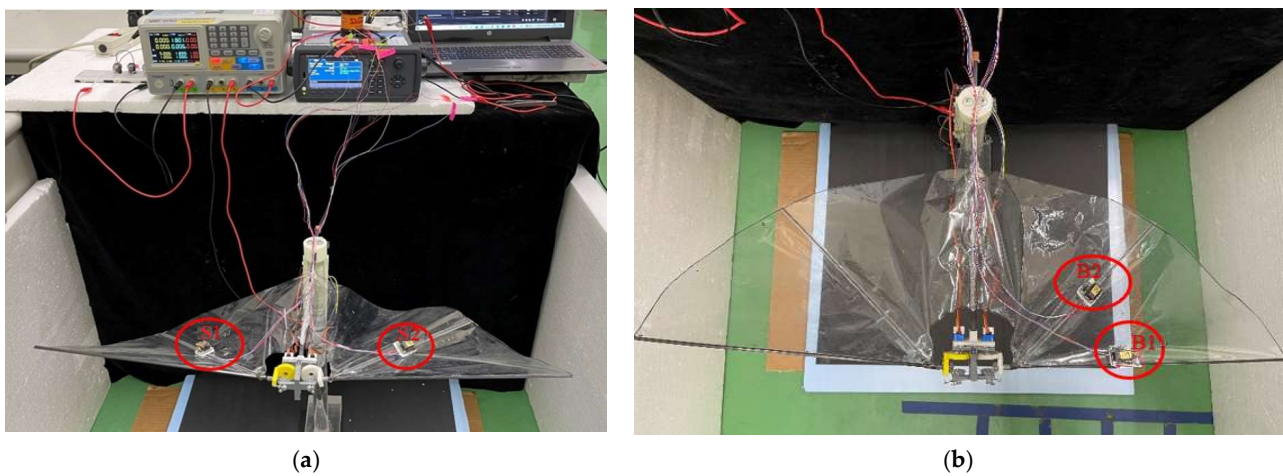


**Figure 5.** Testing of CMOS MEMS flow sensors on flapping wings: (a) flow sensors S1 and S2 on the mean aerodynamic chord (m.a.c.) of both wings (configuration A1); (b) flow sensors B1 and B2 on the leading edge and the m.a.c. of the left wing (configuration A2).

### 3. Results and Discussions

The flapping wings underwent independent control through a pair of servo motors and maintained a flapping frequency of below 2 Hz [1]. After the conversion of the signal by using Equation (3), the local flow speed was obtained corresponding to different frequencies from 1.23 to 1.6 Hz. The response of sensors S1 and S2 on flapping wing configuration A1 is shown in Figure 6 and sensors B1 and B2 on flapping wing configuration A2 is shown in Figure 7. Due to the limited capability of DAQ (1000 scans per second), the data with large noise were captured. By processing the low-pass filtering with the cut-off frequency of 45 Hz on the raw data, better sensor signals were obtained, which are shown in Figures 6 and 7.

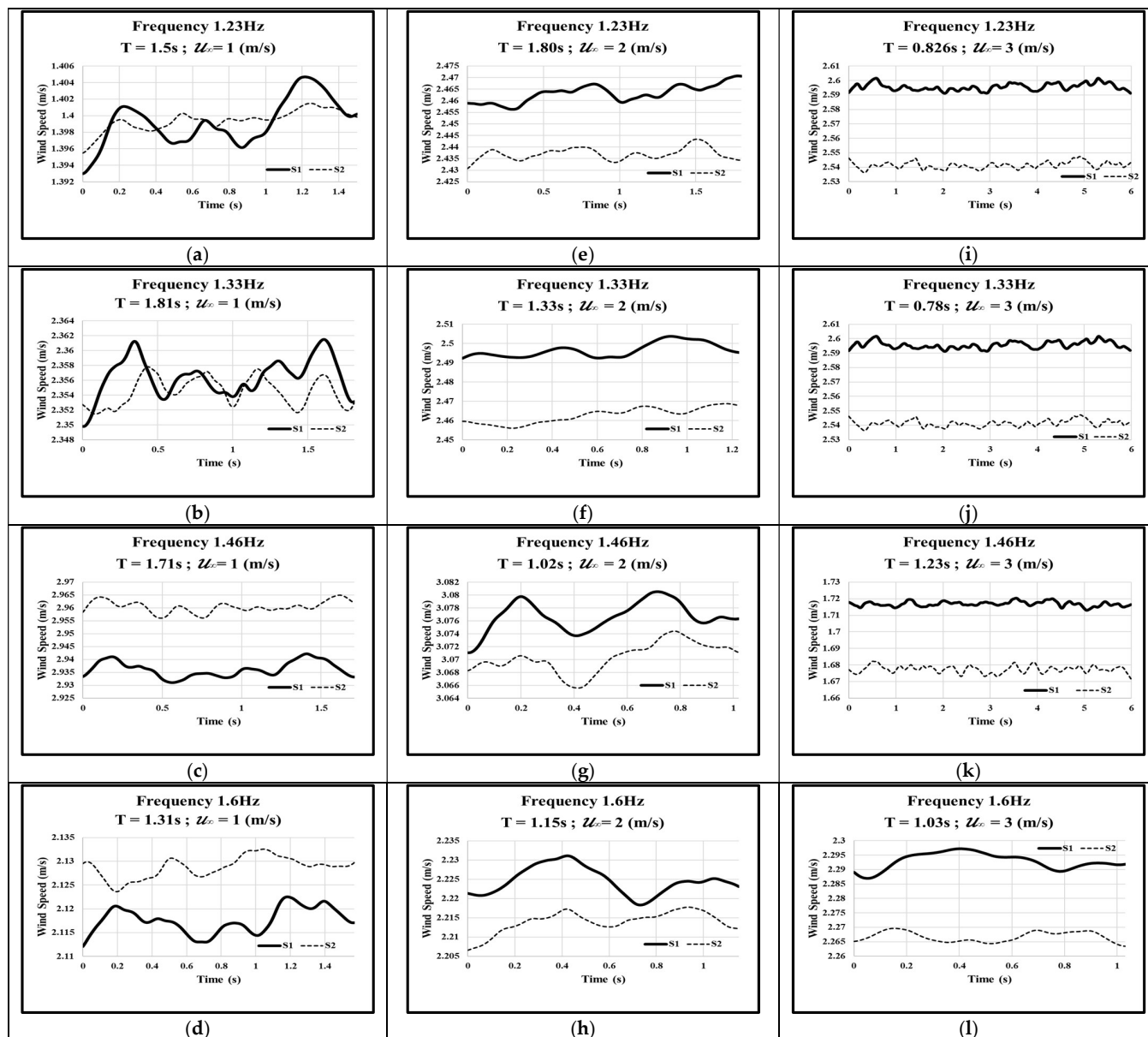


**Figure 6.** For the CMOS MEMS flow sensor configuration A1 with S1 and S2 with each period “T”: (a–d) interpreted values about  $u$  subject to the freestream speed of 1 m/s; (e–h) interpreted values about  $u$  subject to the freestream speed of 2 m/s; (i–l) interpreted values about  $u$  subject to the freestream speed of 3 m/s.



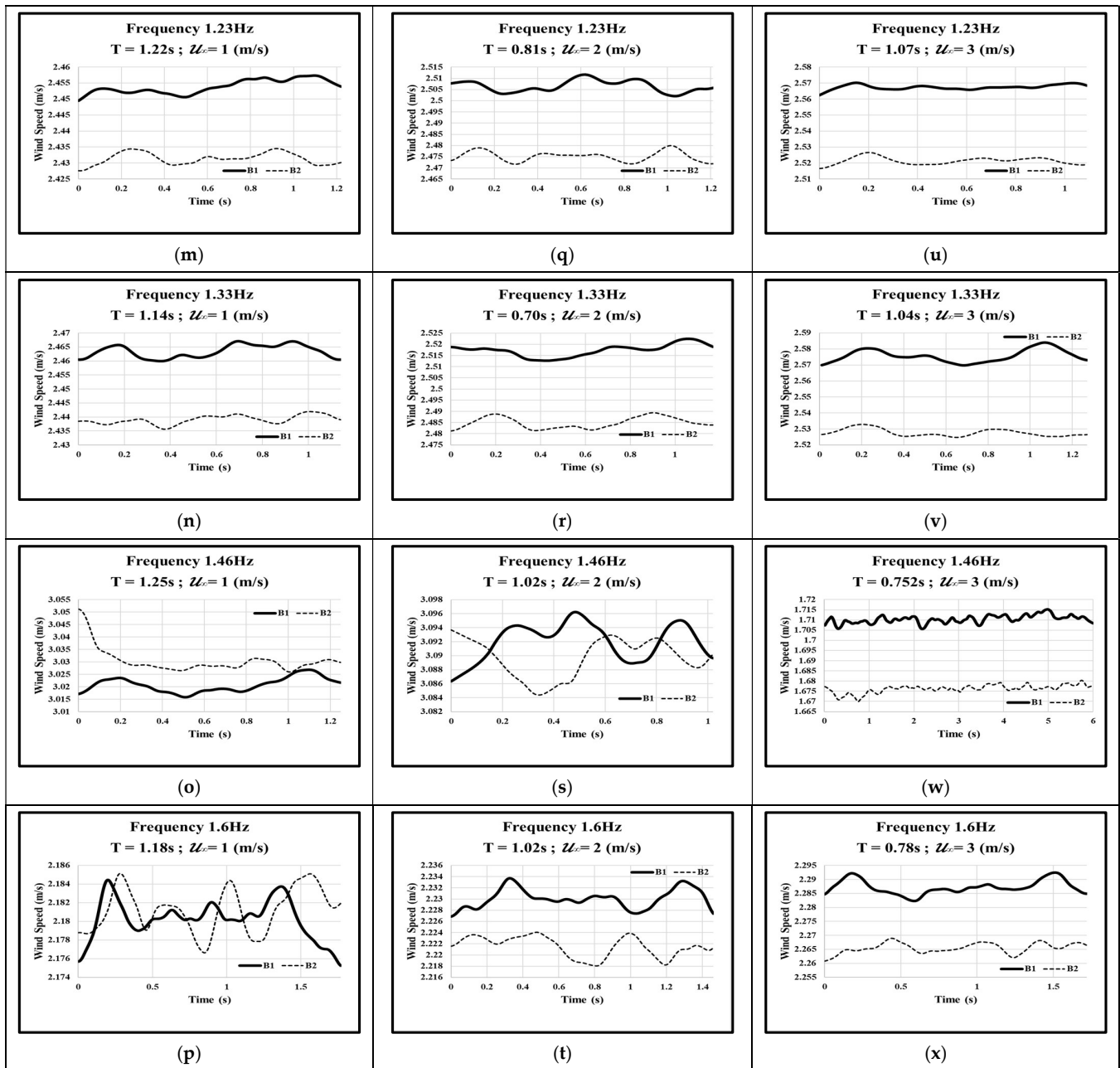


**Figure 7.** For the CMOS MEMS flow sensor configuration A2 with B1 and B2 with each period “T”: (m–p) interpreted values about  $u$  subject to the freestream speed of 1 m/s; (q–t) interpreted values about  $u$  subject to the freestream speed of 2 m/s; (u–x) interpreted values about  $u$  subject to the freestream speed of 3 m/s.

In order to apparently compare the system functions of each sensor, two sensors such as S1 and S2 of configuration A1 with a symmetrical mounting configuration and their output local speeds obtained similar characteristics to each other, as depicted in Figure 6. However, in configuration A2, the B1 sensor output at the leading edge basically followed the trend of sensor B2 at the m.a.c., which is observed in Figure 7. It was due to the phase difference between the leading edge and the m.a.c. that exhibited a rotational behavior during the flapping motion, and it caused the delay phenomenon in the sensor measurements.

In addition, during the consecutive wind tunnel experiments, the data were divided into configurations of (B1/B2) and (S1/S2) as dual sensors. Due to the weight of the sensors (including packaging and placement on two wings), a phase delay was observed in the

signals from the two pairs of outputs. Furthermore, the reason for a phase delay between symmetrical sensors S1 and S2 may happen due to slight differences in the manufacturing of the wing mechanism or the system control's inability to perfectly synchronize the movements of both wings during flapping. On the other hand, the phase delay between the two sensors on the same wing (B1 and B2) was more pronounced from the perspective of the flow field, as one sensor is located at the leading edge and the other at the center of the chord. Additionally, the installation of these two pairs of sensor modules on the wings created a significant load on the wing mechanism during flapping, and it decreased the velocity and AOA.

During the experiments of SOFWs, the sensor output voltages were acquired in the freestream velocity  $u_\infty$  of the wind tunnel from 1 to 3 m/s and, with each set of measurements, obtained a flapping frequency varying from 1.23 to 1.60 Hz. Each of the data measurements corresponded for at least two to three cycles of flapping motion of FWMAVs. The flapping speed is given by

$$u_f = \varnothing bf \quad (4)$$

where the stroke angle  $\varnothing$  is  $90^\circ$ , and  $f$  is the flapping frequency.

Therefore, the flapping speed  $u_f$  varied from 1.35 to 1.76 m/s, corresponding to the flapping frequency  $f$  varied from 1.23 to 1.60 Hz. The total speed or the resultant speed  $u_{res}$  integrated the freestream velocity  $u_\infty$ , and the flapping speed  $u_f$  is given as

$$u_{res} = \sqrt{u_f^2 + u_\infty^2} \quad (5)$$

Based on Equation (5), for the  $u_\infty$  of 1, 2, and 3 m/s, the value of  $u_{res}$  has to be in the range of 1.35~1.76, 2.41~2.66, and 3.29~3.48 m/s, respectively. The resultant speed  $u_{res}$  can be regarded as a range for the data verification of the SOFWs speed values shown in Figures 6 and 7, which ensures the reliability and validity of the experimental data. It was found in Figure 6a,d-f,h of sensor configuration A1 and Figure 7p-r,t of sensor configuration A2 that they obtained speed values within the estimated range of  $u_{res}$  reasonably. All these accepted cases happened particularly in the freestream wind speed range below or equal to 2 m/s. The SOFWs data shown in Figure 8 were compared with the lift and the net thrust signal generated by the force gauge of the wind tunnel depicted in Figure 4.

Comparing the time-varying speeds of the SOFWs depicted in Figure 8a,p,t with the waveforms shown in Figure 8(a1,a2,p1,p2,t1,t2) of the force gauge, it can be observed that the changing characteristics of the SOFW waveform are more similar to the waveform of the net thrust force, especially in the cases of Figure 8a/(a2), Figure 8p/(p2), and Figure 8t/(t2).

Even though the CMOS MEMS flow sensors on flapping wings can detect the dynamic flow information related to the net thrust forces accordingly, the waveforms from the flow sensors and the force gauge are still not identical in Figure 8. Furthermore, the phase lag can also be observed in configurations S1/S2 in Figure 8a/(a2) and configurations B1/B2 in Figure 8p/(p2) and Figure 8t/(t2).

In summary, the performance of the flow sensors was measured from the flapping behavior of the FWMAVs, and there are two aspects that can be improved in the future. Firstly, the noise in the mechanism, even the flapping wing behavior filtering post-processing or the system control, is still an issue of the sensor that has to be improved. Secondly, the total weight of the sensor packaged module is too heavy, which creates a significant load that greatly impacts data accuracy during measurements. Consequently, miniaturizing the sensor or monolithic integration of the SOFWs remains an important goal for the future.

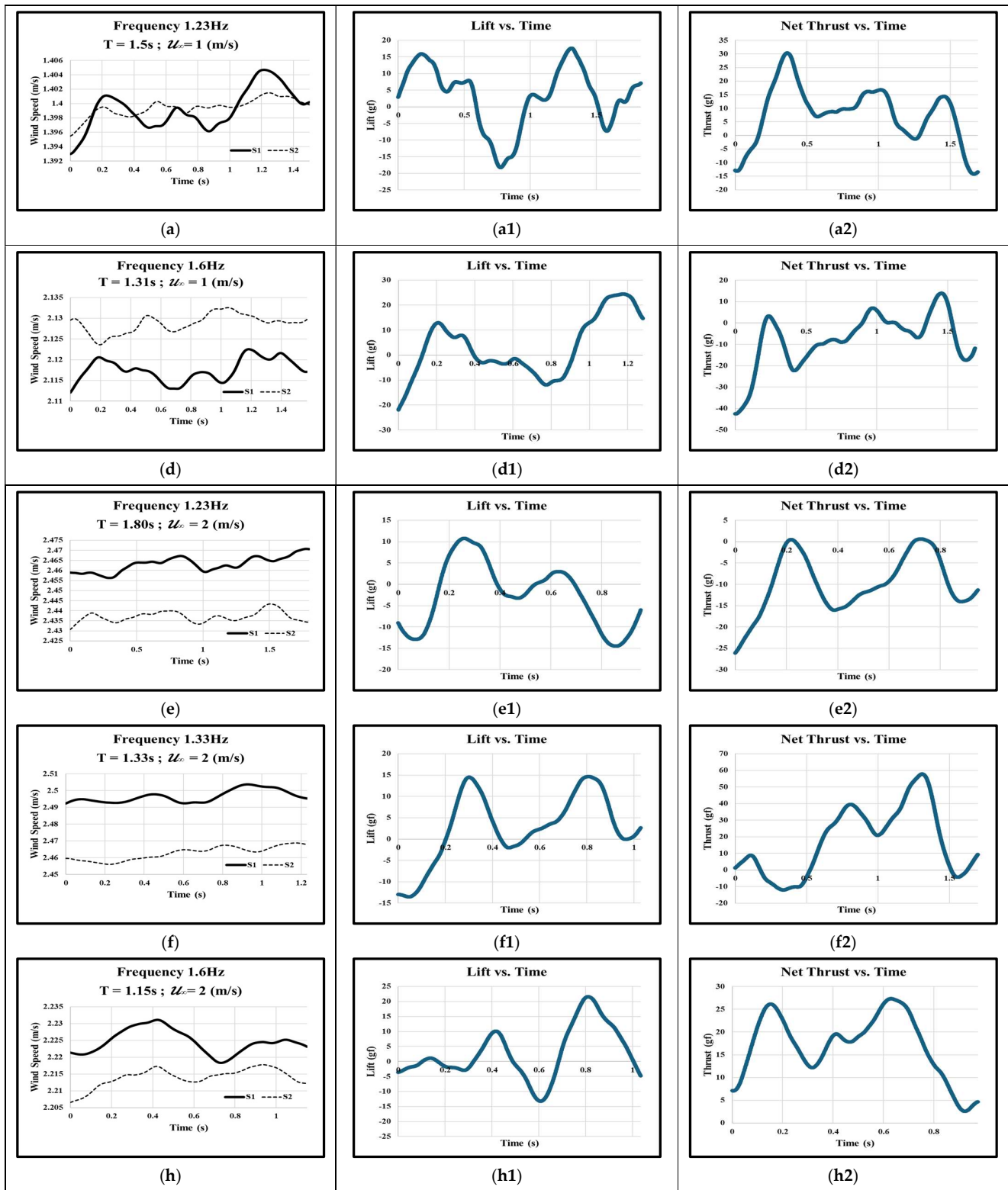
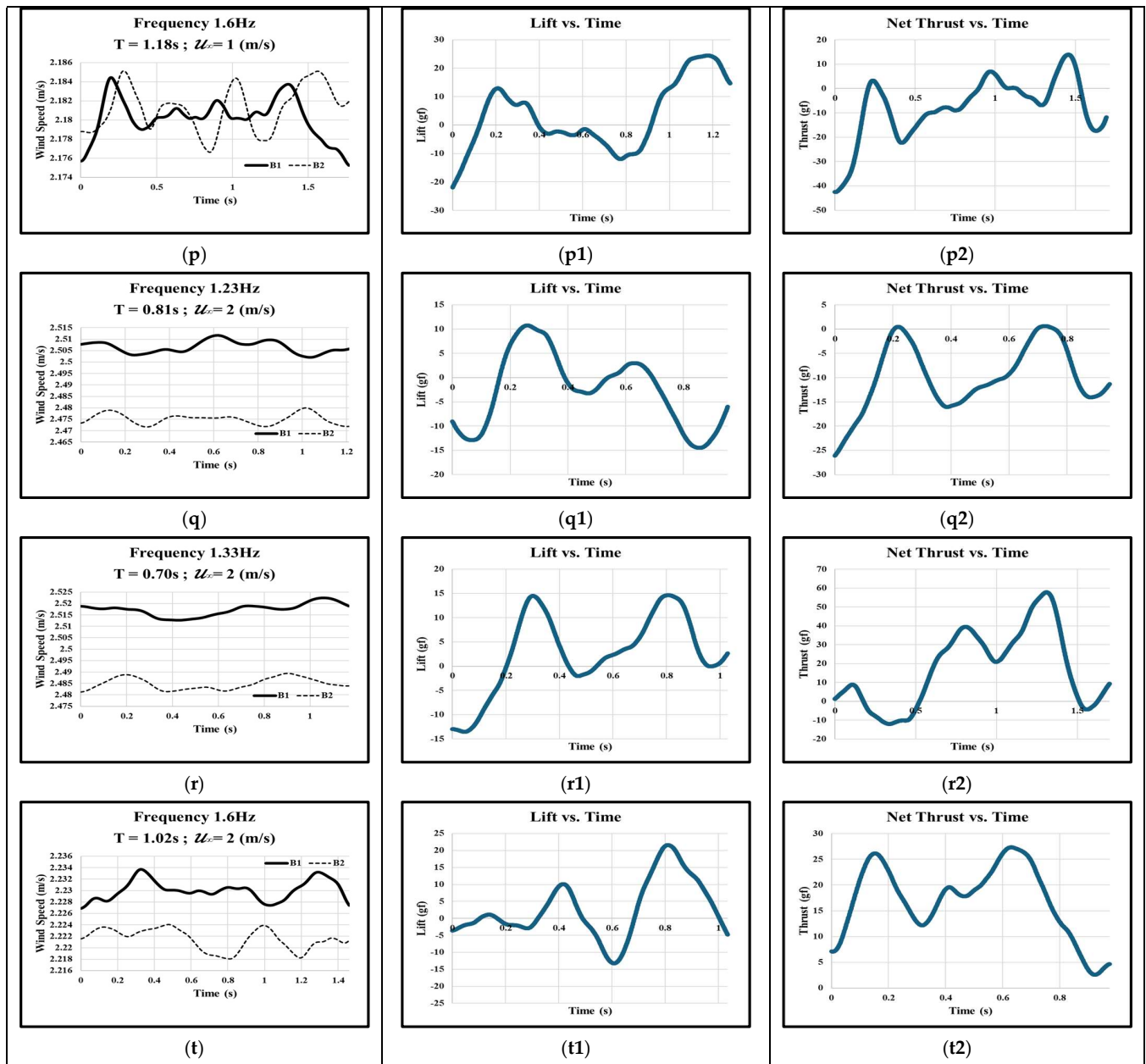


Figure 8. Cont.



**Figure 8.** (a,d–f,h) Interpreted values about  $u$  of the CMOS MEMS flow sensors of configuration A1 within a reasonable range; (p–r,t) interpreted values about  $u$  of the CMOS MEMS flow sensors of configuration A1 within a reasonable range; (a1–t1) lift forces measured by force gauge; (a2–t2) net thrust forces measured by force gauge.

#### 4. Conclusions

The innovative concept of sensors on flapping wings (SOFWs) was successfully demonstrated for the first time on a 70-cm-span servo-actuated flapping wing. The sensitivity of the CMOS MEMS flow sensor with parylene packaging was calibrated using a nonlinear empirical formula, yielding an equivalent sensitivity of  $-3.24 \text{ mV/V}/(\text{m/s})$  for flow speeds below 6 m/s. CMOS MEMS flow sensors installed at the leading edge or the mean aerodynamic chord (m.a.c.) of the flapping wing produced identifiable signals, although a data filtering process was required. The interpreted flow speed signals exhibited a similar behavior to the (net) thrust force exerted on the flapping wing under freestream wind speeds of 2 m/s or less. For future improvements to the SOFWs experiments, simplification

of the signal processing and monolithic integration of MEMS sensors with the flapping wings are recommended.

**Author Contributions:** Conceptualization, L.-J.Y.; methodology, L.-J.Y., W.-C.W. and B.E.; validation, L.-J.Y., W.-C.W., C.T. and B.E.; formal analysis, L.-J.Y., W.-C.W., C.T., B.E. and M.I.S.; investigation and resources, L.-J.Y., W.-C.W., C.T. and B.E.; data curation, W.-C.W., C.T. and M.I.S.; writing—original draft preparation, W.-C.W.; writing—review and editing, L.-J.Y., C.T. and B.E.; visualization, M.I.S.; supervision, L.-J.Y.; project administration, L.-J.Y.; funding acquisition, L.-J.Y. All authors have read and agreed to the published version of the manuscript.

**Funding:** This work is supported by Taiwan’s National Science and Technology Council (NSTC) by the project grant number 112-2221-E-032-043-MY2.

**Institutional Review Board Statement:** Not applicable.

**Informed Consent Statement:** Not applicable.

**Data Availability Statement:** Dataset available on request from the authors.

**Acknowledgments:** The TSRI free foundry service to academics in Taiwan is fully appreciated. The medium-sized wind tunnel testing provided by J.-X. Wu, Civil Engineering, Tamkang University, is also highly appreciated.

**Conflicts of Interest:** The authors declare no conflicts of interest.

## References

1. Pornsinsirirak, T.N.; Tai, Y.C.; Nassef, H.; Ho, C.M. Titanium-alloy MEMS wing technology for a micro aerial vehicle application. *Sens. Actuators A Phys.* **2001**, *89*, 95–103. [[CrossRef](#)]
2. De Croon, G.C.A.; Groen, M.A.; de Wagter, C.; Remes, B.; Ruijsink, R.; van Oudheusden, B.W. Design, aerodynamics and autonomy of the DeFly. *Bioinspir. Biomim.* **2012**, *7*, 025003. [[CrossRef](#)] [[PubMed](#)]
3. Keennon, M.; Klingebiel, K.; Won, H.; Andriukov, A. Tailless flapping wing propulsion and control development for the nano hummingbird micro air vehicle. In Proceedings of the American Helicopter Society Future Vertical Lift Aircraft Design Conference 2012, San Francisco, CA, USA, 18–20 January 2012; pp. 1–24.
4. Phan, H.V.; Park, H.C. Mechanisms of collision recovery in flying beetles and flapping-wing robots. *Science* **2020**, *370*, 1214–1219. [[CrossRef](#)] [[PubMed](#)]
5. Ashraf, M.; Young, J.; Lai, J. Reynolds number, thickness and camber effects on flapping airfoil propulsion. *J. Fluids Struct.* **2011**, *27*, 145–160. [[CrossRef](#)]
6. Ismail, N.; Zulkifli, A.; Abdullah, M.; Basri, M.H.; Abdullah, N.S. Optimization of aerodynamic efficiency for twist morphing MAV wing. *Chin. J. Aeronaut.* **2014**, *27*, 475–487. [[CrossRef](#)]
7. Flint, T.J.; Jeremy, M.C.; New, T.H.; Ho, W.H. Computational study of a pitching bio-inspired corrugated airfoil. *Int. J. Heat Fluid Flow* **2017**, *65*, 328–341. [[CrossRef](#)]
8. Li, H.; Nabawy, M.R.A. Effect of stroke amplitude and wing platform on the aerodynamic performance of hovering flapping wing. *Aerospace* **2022**, *9*, 479. [[CrossRef](#)]
9. Yang, L.J.; Esakki, B. *Flapping Wing Vehicles: Numerical and Experimental Approach*; CRC Press: Boca Raton, FL, USA, 2021; pp. 49–75.
10. Ramasamy, M.; Leishman, J.G. Phase-locked particle image velocimetry measurements of a flapping wing. *J. Aircr.* **2006**, *43*, 1867–1875. [[CrossRef](#)]
11. Rivera, M.K.; Aluie, H.; Ecke, R.E. The direct enstrophy cascade of two-dimensional soap film glows. *Phys. Fluids* **2014**, *26*, 055105. [[CrossRef](#)]
12. Pong, K.C.; Ho, C.M.; Liu, J.; Tai, Y.C. Non-linear pressure distribution in uniform microchannels. *Am. Soc. Mech. Eng. Fluids Eng. Div.* **1994**, *197*, 51–56.
13. Liu, J.; Tai, Y.C.; Ho, C.M. MEMS for pressure distribution studies of gaseous flows in microchannels. In Proceedings of the 8th IEEE MEMS 1995, Amsterdam, The Netherlands, 29 January–2 February 1995; pp. 209–215.
14. Jiang, F.; Tai, Y.C.; Ho, C.M.; Karan, R.; Garstener, M. Theoretical and experimental studies of micromachined hot-wire anemometers. In Proceedings of the Technical Digest—International Electron Devices Meeting 1994, San Francisco, CA, USA, 11–14 December 1994; pp. 139–142.

15. Pornsinsirak, T.N.; Liger, M.; Tai, T.-C.; Ho, S.; Ho, C.-M. Flexible parylene-valved skin for adaptive flow control. In Proceedings of the 15th IEEE MEMS Conference, Las Vegas, NV, USA, 20–24 January 2002; pp. 101–104.
16. Jiang, F.; Lee, G.B.; Tai, Y.C.; Ho, C.M. A flexible micromachine-based shear-stress sensor array and its application to separation-point detection. *Sens. Actuators A Phys.* **2000**, *79*, 194–203. [[CrossRef](#)]
17. Lee, G.B.; Shih, C.; Tai, Y.C.; Tsao, T.; Ho, C.M. Robust vortex control of a delta wing using distributed MEMS actuators. *J. Aircr.* **2000**, *37*, 697–706. [[CrossRef](#)]
18. Xu, Y.; Jiang, F.; Newbern, S.; Huang, A.; Ho, C.M.; Tai, Y.C. Flexible shear-stress sensor skin and its application to unmanned aerial vehicles. *Sens. Actuators A Phys.* **2003**, *105*, 321–329. [[CrossRef](#)]
19. Javed, Y.; Mansoor, M.; Shah, I.A. A review of principles of MEMS pressure sensing with its aerospace applications. *Sens. Rev.* **2019**, *39*, 652–664. [[CrossRef](#)]
20. Nguyen, N. Micromachined flow sensors—A review. *Flow Meas. Instrum.* **1997**, *8*, 7–16. [[CrossRef](#)]
21. Dalola, S.; Cerimovic, S.; Kohl, F.; Beigelbeck, R.; Schalko, J.; Ferrari, V. MEMS thermal flow sensor with smart electronic interface circuit. *IEEE Sens. J.* **2012**, *12*, 3318–3328. [[CrossRef](#)]
22. Wu, C.H.; Kang, D.; Chen, P.-H.; Tai, Y.C. MEMS thermal flow sensors. *Sens. Actuators A Phys.* **2016**, *241*, 135–144. [[CrossRef](#)]
23. Ahmed, M.; Xu, W.; Mohamad, S.; Duan, M.; Lee, Y.K.; Bermak, A. Integrated CMOS-MEMS flow sensor with high sensitivity and large flow range. *IEEE Sens. J.* **2017**, *17*, 2318–2319. [[CrossRef](#)]
24. Huang, L. Micromachined thermal time-of-flight flow sensors and their applications. *Micromachines* **2022**, *13*, 1729. [[CrossRef](#)]
25. Xu, W.; Pan, L.; Gao, B.; Chiu, Y.; Xu, K.; Lee, Y.K. Systematic study of packaging designs on the performance of CMOS thermoresistive micro calorimetric flow sensors. *J. Micromech. Microeng.* **2017**, *27*, 085001. [[CrossRef](#)]
26. Dumstorff, G.; Brauns, E.; Lang, W. Investigations into packaging technology for membrane-based thermal flow sensors. *J. Sens. Sens. Syst.* **2015**, *4*, 45–52. [[CrossRef](#)]
27. Xu, W.; Gao, B.; Lee, Y.K.; Chiu, Y. Packaging effect on the flow separation of CMOS thermoresistive micro calorimetric flow sensors. In Proceedings of the IEEE 11th Annual International Conference on Nano/Micro Engineered and Molecular Systems (NEMS) 2016, Sendai, Japan, 17–20 April 2016; pp. 62–65.
28. Yang, L.J.; Tasupalli, C.; Wang, W.C.; Lee, C.Y.; Lee, C.Y.; Athikary, K.G.; Wu, J.X. Initial study of the onsite measurement of flow sensors on turbine blades (SOTB). *Micromachines* **2024**, *15*, 877. [[CrossRef](#)] [[PubMed](#)]
29. Dai, C.L.; Lu, S.S.; Chang, P.Z. Design and processing of integrated micro accelerometers using standard CMOS process. *J. Chin. Inst. Eng.* **1997**, *20*, 47–55. [[CrossRef](#)]
30. Qu, H. CMOS MEMS fabrication technologies and devices. *Micromachines* **2016**, *7*, 14. [[CrossRef](#)] [[PubMed](#)]
31. Yang, L.J.; Waikhom, R.; Shih, H.Y.; Lee, Y.K. Foundry service of CMOS MEMS process and case study of flow sensors. *Processes* **2022**, *10*, 1280. [[CrossRef](#)]
32. Yang, L.J.; Joseph, V.J.; Lo, Y.L.; Tang, W.T.; Esakki, B.; Kompala, S.; Veeranjaneyulu, P. Aerodynamic evaluation of flapping wings with leading-edge twisting. *Biomimetics* **2023**, *8*, 134. [[CrossRef](#)]
33. Roskam, J. *Airplane Flight Dynamics and Automatic Flight Control*; Roskam Aviation and Engineering Corp.: Lawrence, KS, USA, 1979; pp. 69–78.

**Disclaimer/Publisher’s Note:** The statements, opinions and data contained in all publications are solely those of the individual author(s) and contributor(s) and not of MDPI and/or the editor(s). MDPI and/or the editor(s) disclaim responsibility for any injury to people or property resulting from any ideas, methods, instructions or products referred to in the content.